

Alma Mater Studiorum Università di Bologna
Archivio istituzionale della ricerca

Toward a Compact Wireless Surface Acoustic Wave Pirani Microsensor with Extended Range and Sensitivity

This is the final peer-reviewed author's accepted manuscript (postprint) of the following publication:

Published Version:

Toto S., Nicolay P., Morini G.L., Voigt A., Korvink J.G., Brandner J.J. (2021). Toward a Compact Wireless Surface Acoustic Wave Pirani Microsensor with Extended Range and Sensitivity. *HEAT TRANSFER ENGINEERING*, 42(6), 565-578 [10.1080/01457632.2019.1707409].

Availability:

This version is available at: <https://hdl.handle.net/11585/850978> since: 2022-02-01

Published:

DOI: <http://doi.org/10.1080/01457632.2019.1707409>

Terms of use:

Some rights reserved. The terms and conditions for the reuse of this version of the manuscript are specified in the publishing policy. For all terms of use and more information see the publisher's website.

This item was downloaded from IRIS Università di Bologna (<https://cris.unibo.it/>).
When citing, please refer to the published version.

(Article begins on next page)

This is the final peer-reviewed accepted manuscript of:

S. Toto et al.

Toward a Compact Wireless Surface Acoustic Wave Pirani Microsensor with Extended Range and Sensitivity

in *Heat Transfer Engineering*, vol. 42, no. 6, pp. 565-578

The final published version is available online at:

<https://doi.org/10.1080/01457632.2019.1707409>

Rights / License:

The terms and conditions for the reuse of this version of the manuscript are specified in the publishing policy. For all terms of use and more information see the publisher's website.

This item was downloaded from IRIS Università di Bologna (<https://cris.unibo.it/>)

When citing, please refer to the published version.

Toward a Compact Wireless Surface Acoustic Wave Pirani Microsensor with Extended Range and Sensitivity

Sofia Toto, Pascal Nicolay, Gian Luca Morini, Achim Voigt, Jan G. Korvink, and Juergen J. Brandner

QUERY SHEET

This page lists questions we have about your paper. The numbers displayed at left are hyperlinked to the location of the query in your paper.

The title and author names are listed on this sheet as they will be published, both on your paper and on the Table of Contents. Please review and ensure the information is correct and advise us if any changes need to be made. In addition, please review your paper as a whole for typographical and essential corrections.

Your PDF proof has been enabled so that you can comment on the proof directly using Adobe Acrobat. For further information on marking corrections using Acrobat, please visit <http://journalauthors.tandf.co.uk/production/acrobat.asp>; <https://authorservices.taylorandfrancis.com/how-to-correct-proofs-with-adobe/>

The CrossRef database (www.crossref.org/) has been used to validate the references.

AUTHOR QUERIES

No Queries

Toward a Compact Wireless Surface Acoustic Wave Pirani Microsensor with Extended Range and Sensitivity

Sofia Toto^a, Pascal Nicolay^b, Gian Luca Morini^c, Achim Voigt^a, Jan G. Korvink^a, and Juergen J. Brandner^a

^aInstitute of Microstructure Technology, Karlsruhe Institute of Technology, Eggenstein-Leopoldshafen, Germany; ^bCarinthia Institute for Smart Materials and Manufacturing Technologies, Carinthia University of Applied Sciences, Villach, Austria; ^cDipartimento di Ingegneria Industriale, Alma Mater Studiorum Università di Bologna, Bologna, Italy

ABSTRACT

A wireless vacuum sensor based on the Pirani principle and Surface Acoustic Waves (SAW) has been designed, simulated and manufactured. The sensing unit is a heat conductivity gauge based on a passive SAW temperature sensor. The required heating energy is applied to the sensor by means of inductive coupling whereas the measurement signal is sent via a ceramic antenna. The sensor is a compact polymer cube containing all the units and operating completely wireless. Simulation was used to design and optimize the behavior of the sensor in vacuum and to predict the performances of the sensor. It was followed by the manufacturing and the assembly of a prototype. This communication presents the design, the simulation results and the manufacturing steps of the prototype.

Background

Subatmospheric pressure sensors are bulky and demand much effort to be integrated inside vacuum chambers. Vacuum transducers have limited sensing ranges and usually, several devices are needed to measure the complete targeted range. Microfluidics devices have proven to be efficient devices for sensing and heat transfer applications at the macro scale [1].

The Pirani principle is commonly used to sense pressure in the fine and rough vacuum range. It is based on the heat transfer between a heated sensing element (wire, plate or chip) and its surrounding gas molecules. The temperature variation of the sensor depends on the number of gas molecules and therefore on the pressure. In practice, the sensing element is inserted inside a Wheatstone bridge and the temperature variation is transduced into a resistance variation [2].

The Pirani principle is based on the collisions occurring between the gas molecules inside a chamber and the walls of the sensing element. This phenomenon is modeled by the gas kinetic theory [3]. The number of collisions and the efficiency of this phenomenon as a pressure sensing principle depend on the flow regime i.e. the Knudsen number, which is defined as:

$$Kn = \frac{l}{d} \quad (1)$$

where l is the mean free path of the gas and d the characteristic dimension of the chamber. The Knudsen number estimates the ratio of intermolecular collisions to collisions between the walls and the molecules. From the value of this ratio, different flow regimes can be identified.

When the value of Kn is higher than 10, the mean free path is much higher than the chamber dimensions and there are very few molecules in the chamber. When Kn is below 0.001 the intermolecular collisions are overwhelming the collisions between the walls and the gas molecules. Intermediate values of the Knudsen number between 0.001 and 10 are desired, corresponding to the slip and transition flow regimes where the collisions between the gas molecules and the walls are sufficient to be measured. Therefore, in the slip and transition flow regimes, the gas thermal conductivity strongly depends on pressure [3].

Surface Acoustic Waves (SAW) propagate on the surface of piezoelectric crystals. An Interdigital Transducer (IDT) which is a set of metallic electrodes etched on the surface of piezoelectric substrates, converts voltage into waves back and forth [4].

Nomenclature

AC	alternative current	r	The resistivity, Ω m
C	Elasticity coefficient of the piezoelectric crystal, Pa	RMS	Root Mean Square
C_p	The specific heat capacity, $J\ kg^{-1}\ K$	R_x	Receiving circuit
COM	Coupling of modes	S_i	The surface of each face of the chip, m^2
d	Characteristic dimension of a channel, m	SAW	Surface Acoustic Wave
DC	Direct current	T	Temperature, K
f_r	Resonance frequency of a SAW device, Hz	t	The thickness of a wire, m
FEM	Finite Element Method	T_0	Reference temperature, K
h	The length of the wire, m	TC_{f1}	Temperature coefficient of frequency of the SAW
$h1$	The dielectric thickness, m	T_x	Transmitting circuit
IDT	Interdigital Transducer	u	The fluid velocity, $m\ s^{-1}$
k	The thermal conductivity, $W\ m^{-1}\ K^{-1}$	V	SAW propagation velocity, $m\ s^{-1}$
Kn	Knudsen number of a fluid flow	w	The width of a wire, m
l	Mean free path of a gas molecule, m	z_0	The single ended impedance, Ω
MOSFET	Metal Oxide Semiconductor Field Effect Transistor		
NMOSFET	n-type Metal Oxide Semiconductor Field Effect Transistor		
p	Pitch of the electrodes, m		
PCB	Printed Circuit Board		
PMMA	Polymethyl methacrylate		
PTFE	Polytetrafluoroethylene		
Q	The heating power per unit volume provided at the bottom of the chip, $W\ m^{-3}$		
$q_{r,out}$	The outward heat flux, W		
Q_r	The heating power dissipated via radiation per unit volume, $W\ m^{-3}$		
R	The resistance, Ω		

Greek symbols

Δf	Frequency shift, Hz
ϵ	Surface emissivity of Lithium Niobate compared to the emissivity of a black body
ϵ_{r0}	Dielectric constant
λ	Surface Acoustic Wave wavelength, m
ρ	Density of the crystal, $kg\ m^{-3}$
σ	The Stefan-Boltzmann constant, $W\ m^{-2}\ K^{-4}$
τf	Time, s

An IDT consists of two interlocking comb-shaped metallic coatings on top of a piezoelectric substrate that effectively convert applied radio frequency electrical pulses to mechanical energy and vice versa. The electrical pulses create an electric field at the electrodes of the IDT that generates a mechanical displacement of atoms [5].

The electrical pulses are generated by radio frequency circuits and can be transmitted in a wireless way via antennas. This enables the wireless operation of SAW devices.

Besides, SAW are sensitive to the environment properties. A heated material is subject to thermal expansion, which modifies its physical properties including elasticity, piezoelectricity and permittivity. The variation of those properties is mostly expressed as a Taylor series expansion. At the first order, the sensitivity of the resonance frequency f_r of a piezoelectric crystal to the temperature around a reference temperature T_0 is expressed by the coefficient TC_{f1} (in ppm/K):

$$\frac{\Delta f}{f_r(T_0)} = TC_{f1}(T - T_0) \quad (2)$$

where $f_r(T_0)$ is the resonance frequency at the initial conditions, prior to any thermal expansion. The coefficient TC_{f1} can be as high as 100 ppm/K [4] for Lithium Niobate, which makes SAW devices very accurate temperature sensors. The variation of

resistance of a heated Pirani sensor inside a Wheatstone bridge can be replaced by the variation of the resonance frequency of a heated SAW device in vacuum. The resonant frequency f is defined by [5]:

$$f = \frac{V}{\lambda} \quad (3)$$

where V is the wave propagation velocity and λ the wavelength which depends on the electrodes pitch p according to the relation:

$$\lambda = 2p \quad (4)$$

The velocity of the wave V is expressed as:

$$V = \sqrt{\frac{C}{\rho}} \quad (5)$$

where C is an elasticity coefficient and ρ the density of the material. When the temperature changes, C , ρ and λ are all modified, inducing a modification of the resonance frequency.

The development of inductive coupling for wireless power transfer in many domestic applications allowed to increase the coupling distance between the transmitting and receiving coil of up to 4 cm all along the miniaturization of the coupled coils. The Qi standard for instance refers to low power inductive transfers below 5 W for coupling distances of up to 4 cm between 2 planar coils that can reach 75% of coupling

efficiency [6]. In the case of a passive receiver that needs constant power, only a capacitor is needed to tune the resonance frequency which makes the receiver circuit relatively small and simple.

In the wake of the concept of the SAW-Pirani for extending the sensing range of vacuum sensors [7–9] and the miniaturization of wireless power transfer systems, the development of a wireless vacuum micro sensor with extended range is discussed. The structural design is followed by the simulation of each component. Then the manufacturing and assembly of the prototype using microfabrication and semiconductor technology is presented.

Sensor design

The sensor consists of a 15 mm by 11 mm by 10 mm polymer box crossed by a 600 μm cylindrical

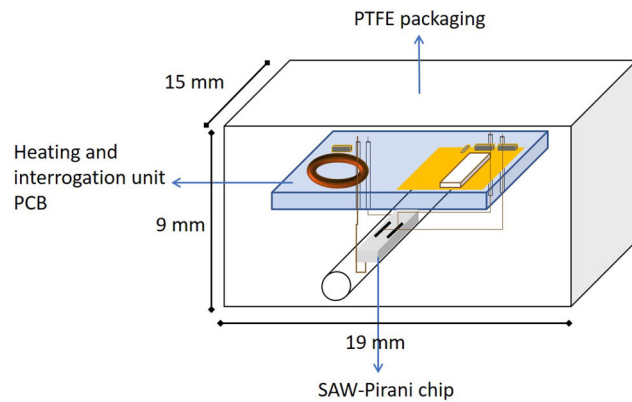


Figure 1. Compact structure of the designed sensor. The polymer package is crossed by a 600 μm cylindric microchannel where the 1 mm by 400 μm by 350 μm sensing chip is located. The 15 mm by 11 mm surface PCB containing the heating and sensing unit is inside the packaging on top of the chip. The PCB contains a coil with its coupled capacitor on the left side and an antenna with its impedance matching elements and its no ground surface on the right side. Holes through the PCB and the packaging allow gold wires to connect the chip to the heating and interrogation units.

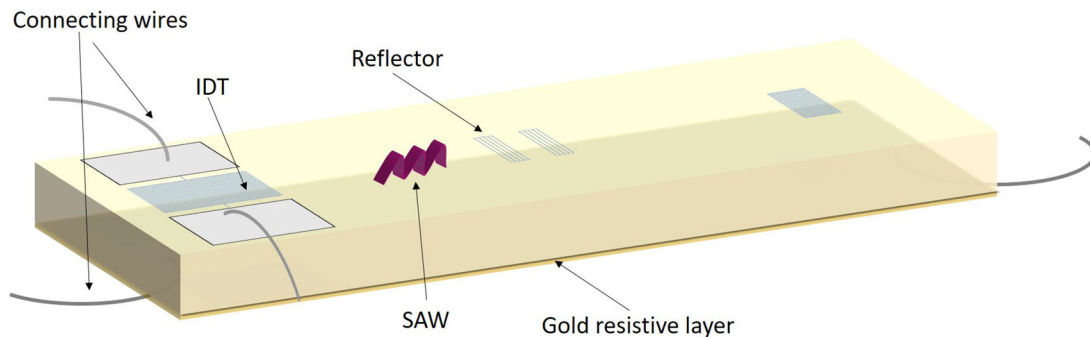


Figure 2. Structure of the designed chip. The Lithium Niobate substrate has a gold resistive layer sputtered and 2 wires for electrical connection at its bottom. On top of the substrate the IDT structure made of the main IDT and 3 reflectors is etched via e-beam lithography. Bonding pads on the top and bottom of the main IDT are electroplated for the electrical connection.

microchannel. The sensing chip is inserted inside the channel and is connected to a heating coil and to an interrogation antenna. Figure 1 shows a schematic of the device. A Printed Circuit Board (PCB) inside the core of the sensor contains the heating unit and the interrogation unit. The heating unit consists mainly of a coil and its coupled capacitor. The interrogation unit consists of an antenna, its transmission line and its impedance matching components. The sensing chip is connected to the heating and interrogation units via wires crossing the packaging through holes.

The polymer housing is made of Polytetrafluoroethylene (PTFE). This material has been selected due to its self-lubricating, electrical insulating and low outgassing properties. Its electrical insulating properties are interesting for wireless operation since it will not absorb the energy radiated to the coil and antenna. The packaging has been designed based on the geometry requirements of the PCB and its components.

The sensing chip has been designed and simulated. It is made out of Y-Z cut Lithium Niobate as a substrate and has dimensions of 6 mm length by 400 μm width by 350 μm thickness. It is a delay line operating at 2.45 GHz which corresponds to a wavelength of 1.3836 μm . The choice of the resonance frequency implies the dimensions of the IDT electrodes according to the Equations (3) and (4). The electrodes are regular with same width and constant pitch. The metallization ratio, which is the fraction of the IDT surface covered with metal equals to 0.5. The main IDT has a width of 41.508 μm and a length of 30.4392 μm . The resolution of the e-beam lithography is 1 nm. The first reflector is located 2 mm away from the main IDT and has 5 fingers. The second reflector is located 2.1920 mm from the main IDT and is identical to the first one. The third and last reflector has 20 fingers and is located 3.920 mm from the main IDT. Figure 2 shows the IDT structure. The



Figure 3. WE-WPCC 760308101216 wireless power charging receiver coil manufactured by Wuerth Elektronik. It can be powered from a distance of up to 2 cm and delivers power of up to 0.11 W. It has a diameter of 6 mm and a height of 2 mm.

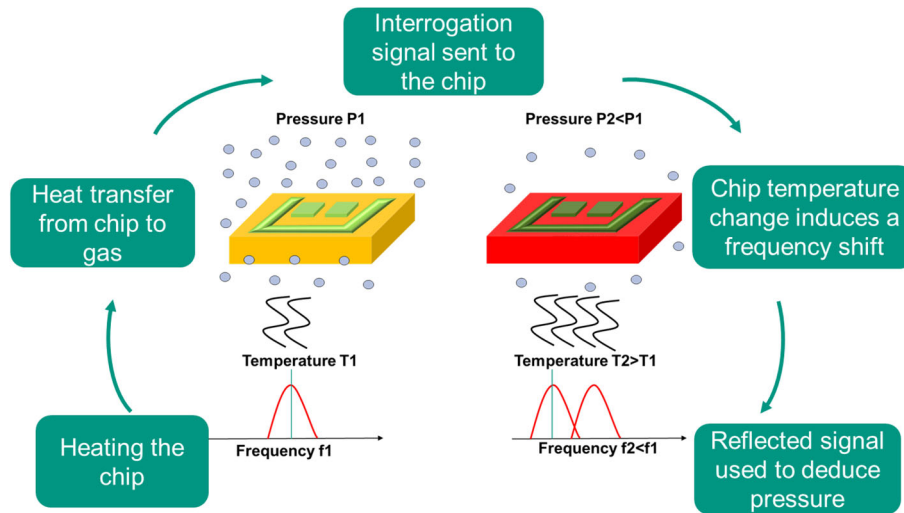


Figure 4. Operating protocol of the sensor: the chip is heated via the gold layer at its bottom that receives current via induction. The heated chip transfers heat to its surrounding gas molecules proportionally to the pressure and its temperature is modified. In parallel the interrogation signal is sent to the chip via the antenna. The temperature change induces a resonance frequency of the chip, the signal reemitted by the antenna contains the resonance frequency that is used to deduce pressure.

aluminum thickness is set at 50 nm as a tradeoff between large reflection coefficient and bulk wave suppression.

The chip is locally heated via a resistive gold layer sputtered at its bottom. A commercial coil was selected that fulfills the requirements of the sensor in terms of power transfer, size, and coupling distance. The chosen coil was the WE-WPCC 760308101216 wireless power charging receiver coil manufactured by Wuerth Elektronik (see Figure 3). It can be powered from a distance of up to 2 cm and delivers power of up to 0.11 W. It has a diameter of 6 mm and a height of 2 mm.

The antenna P/N 2450AT18B100 from Johanson was selected as the interrogation antenna. It operates between 2400 and 2500 MHz and has dimensions of 3.2 mm by 1.6 mm by 1.3 mm and a return loss of -18 dB at its resonance frequency.

The sensor is first inserted into a vacuum environment. Then, the SAW chip inside the microchannel is

heated via the Joule resistance receiving AC current from the coil. The sensing chip will reach an equilibrium temperature after exchanging heat with the surrounding gas molecules. The temperature variation of the chip induces a resonance frequency shift in the case of a resonator structure and changes in echo times in the case of a delay line. The interrogation signal is sent to the sensor via the interrogation antenna using a network analyzer. It is a frequency sweep between 2 GHz and 3 GHz. The minimum of the obtained reflection coefficient S11 values allow to determine the resonance frequency of the chip which depends on the pressure of the gas surrounding the chip. The calibration curve of the resonance frequency vs pressure allows to deduce pressure. Figure 4 shows a schematic of the operating protocol of the sensor.

The behavior of the designed sensor and its components was simulated prior to manufacturing and assembling of a prototype.

Simulation

Several simulations were undertaken in order to determine the dimensions of the chip that would widen its sensing range and to couple the components together.

Thermal simulation of the chip

The dimensions of the chip substrate were set by finite element method (FEM) heat transfer simulations, as well as the energy required to heat the chip. The software COMSOL was used to design the chip geometry and optimize its thermal behavior in vacuum. The Heat Transfer in Solids module was used. It includes heat transfer for solids and fluids. Three components were inserted: the core of the sensor represented by a 1 cm³ Polymethyl methacrylate cube, the sensing chip which is a block of Lithium Niobate and the 600 μm diameter microchannel filled with Nitrogen at different pressures.

The effect of pressure variation was simulated by changing the thermal conductivity of Nitrogen. The values of the thermal conductivity were computed using the model presented in [10] and adapting it to the dimensions of our design. The values of thermal conductivity computed are presented in [9].

The mesh used was a physics controlled mesh from COMSOL, different sizes were tested, leading to the same behavior of the chip. The outside walls of the cube as well as the inlet and outlet of the channel were thermally insulated, the rest of boundaries were all thermal contacts.

Conductive heat transfer and radiative heat transfer were implemented. The surface emissivity of the channel surface was taken as 0.9 which is the emissivity of Polymethyl methacrylate (PMMA), the emissivity of the chip was taken as 0.75, which is the surface emissivity of neat Lithium Niobate, the maximum value that could be reached by the chip emissivity. The equation solved by COMSOL was therefore the heat equation:

$$\rho C_p \frac{\partial T}{\partial \tau} + \nabla \cdot (-k \nabla T) + \rho C_p \mathbf{u} \cdot \nabla T = Q + Q_r \quad (6)$$

where ρ is the density in kg m⁻³, T the temperature in K, τ is the time in seconds, C_p the specific heat capacity (J/kg/K), k is the thermal conductivity in W m⁻¹ K⁻¹, \mathbf{u} is the fluid velocity in m s⁻¹ Q the heating power per unit volume provided at the bottom of the chip in W m⁻³, Q_r is the heating power dissipated via radiation per unit volume in W m⁻³.

Radiation is described by surface to surface radiation between the outer surfaces of the chip and the

inner surface of the channel. The equation of the radiative heat transfer is:

$$q_{r,out} = \sum_{S_i} \varepsilon S_i \sigma (T^4 - T_0^4) \quad (7)$$

where $q_{r,out}$ is the outward heat flux in W, ε the surface emissivity of the chip, S_i is the surface of each face of the chip, σ is the Stefan-Boltzmann constant, T the temperature of the chip surface and T_0 the temperature of the channel which is equal to the ambient temperature. The solver was time dependent from 0 to 100 s with a time step of 0.1 s. The response time being in the range of 60 s, a time step of 0.1 s was deemed reasonable to account for the behavior variations of the sensor.

The chip was heated from its bottom surface with a boundary heat source condition. A power of 10 000 W m⁻² corresponding to 24 mW was continuously provided.

The steady state temperature at the top surface of the chip was observed and recorded. Since the waves propagate on the top surface, the resonance frequency depends on its temperature. The objective was to increase the thermal sensitivity of the chip which means, for different pressures, to increase the steady state temperature difference between the different pressure levels. Figure 5 shows the simulated geometry: it consists of a 1 cm³ cube crossed at its center by a 600 μm diameter cylindric microchannel inside which the chip is suspended without physical contact to the channel. The observed temperature of the chip is uniform.

A parameter sensitivity analysis was conducted to determine the parameters mostly affecting the sensitivity of the chip. The most sensitive thermal parameter is the surface to volume ratio. Indeed, increasing the surface of the chip increases the contact between the gas molecules and the chip and therefore the sensitivity of the device on the one hand. On the other hand, reducing the volume and the thickness reduces the heat capacity of the chip and reduces the response time. Still, the dimensions of the chip need to be set keeping in mind the manufacturing capabilities available and also the mechanical constraints of the chip. A too small thickness would make the chip very fragile. Lithium Niobate wafers with thicknesses of 350 μm being already available off-the shelf, a value of 350 μm thickness was retained. The length and the width of the chip need to fit inside the microchannel, the combination of 6 mm by 400 μm was giving the highest sensitivity compared to the tested values of 200 μm, 300 μm and 600 μm and 6 mm, 7 mm and 8 mm. Figure 6 shows the variation of the temperature

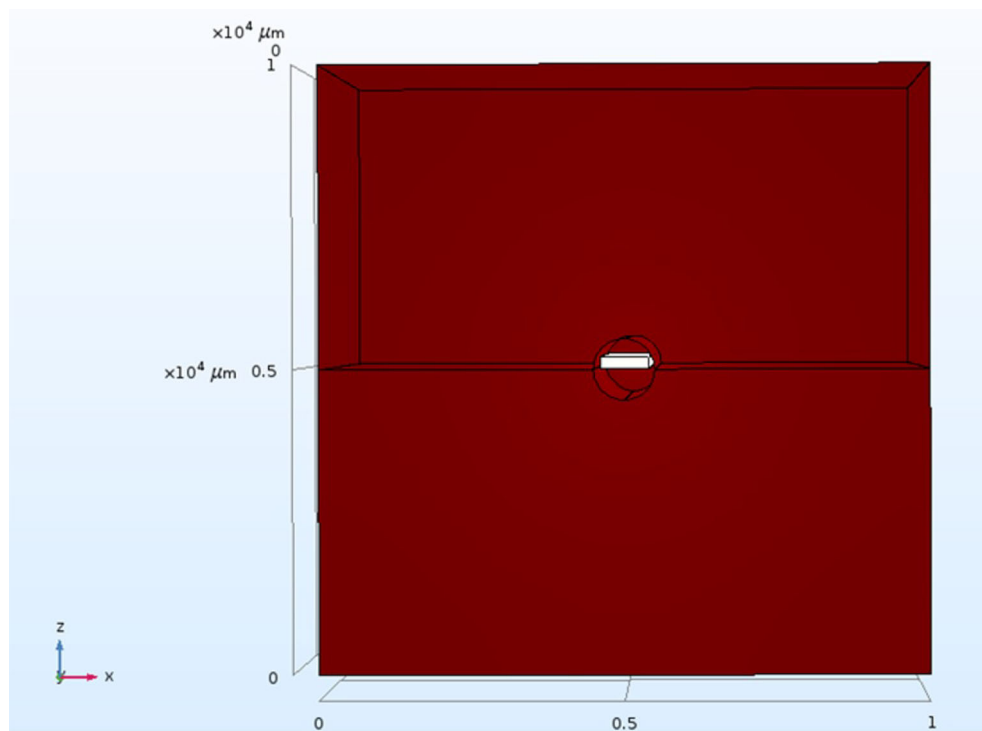


Figure 5. Simulated geometry. A 1 cm^3 PMMA cube is crossed at its center by a $600\text{ }\mu\text{m}$ diameter cylindrical microchannel. The 1 mm by $400\text{ }\mu\text{m}$ by $600\text{ }\mu\text{m}$ chip is suspended inside the microchannel. The x and y axes units are identical.

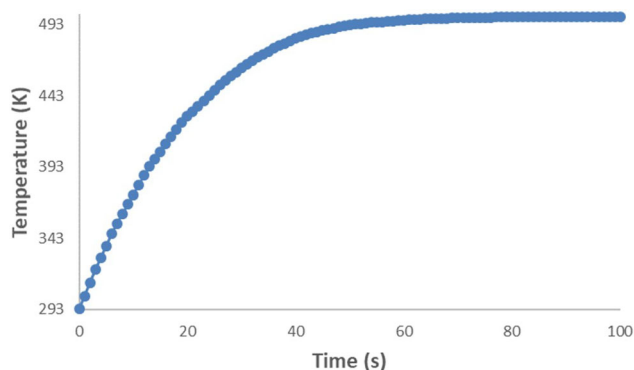


Figure 6. Temperature of the chip vs time at 10^{-4} Pa . The steady state temperature is reached after 38 s.

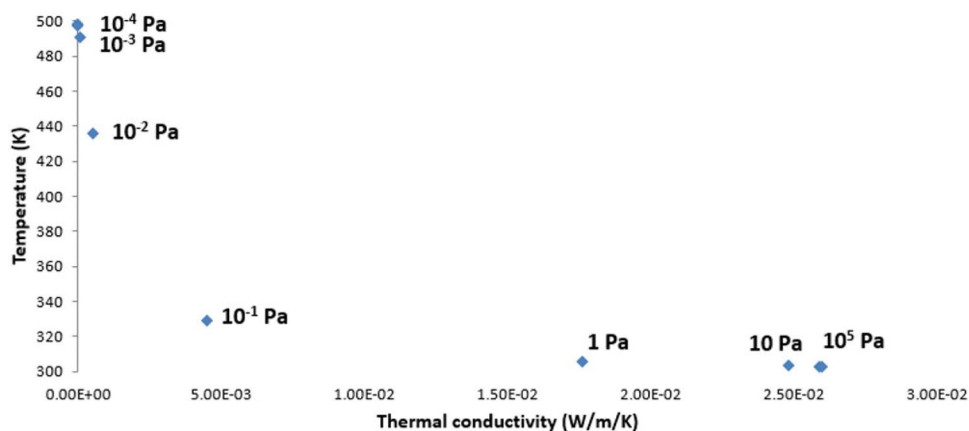


Figure 7. Steady state temperature of the chip in K vs thermal conductivity at different pressures. The thermal conductivity of the gas depends on pressure, which means that the final temperature of the chip also depends on pressure and is used to measure it.

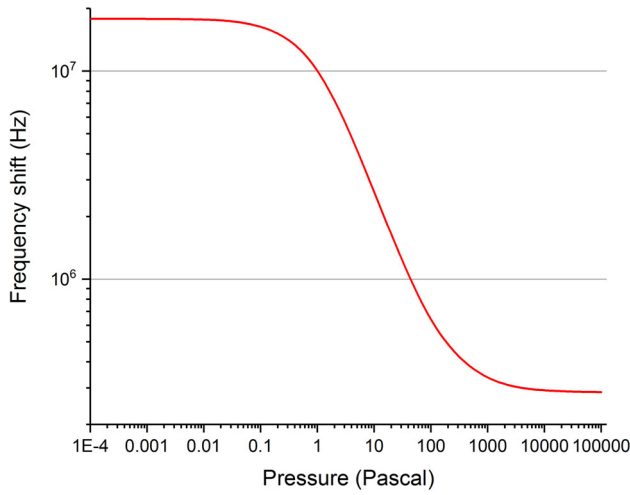


Figure 8. Calculated calibration curve of the sensor. The curve shows the pressure induced frequency shift for an initial pressure of 10^5 Pa and an initial frequency of 2.45 GHz. The characteristic S-shape profile of the thermal conductivity vs pressure can also be observed for the frequency shift but on the opposite direction since the temperature coefficient of frequency is negative.

Table 1. Frequency shift at selected ranges. The frequency shift per decade is in the kHz range or higher and can easily be measured using a Vector Network Analyzer.

Pressure range	Frequency shift
10^{-4} to 10^{-3} Pa	15.435 kHz
10^{-3} to 10^{-2} Pa	152.145 kHz
10^3 to 10^4 Pa	55.125 kHz
10^4 to 10^5 Pa	6.615 kHz

Using a value of the temperature coefficient of frequency TC_{f1} of -100 ppm/K [4] for Lithium Niobate the resonance frequency shift from a 2.45 GHz initial resonance frequency at 300 K was calculated. Figure 8 shows the calibration curve calculated through the whole sensing range. Table 1 shows the frequency shift at selected pressure ranges. The frequency shifts calculated can be measured with a Network Analyzer.

IDT

After the chip dimensions and the delay line structure were set, the time response of the IDT was simulated using Matlab. The IDT was simulated using the Coupling Of Modes (COM) method [11]. The COM parameters were extracted using a FEM model of the elementary cell type and periodic boundary conditions. The P-Matrices method was used to calculate the response of the IDT. An initial 2 mm chip space was set between the IDT and the first reflector to isolate the useful echoes from spurious ones due to the environment. The duration of a reflector pulse was

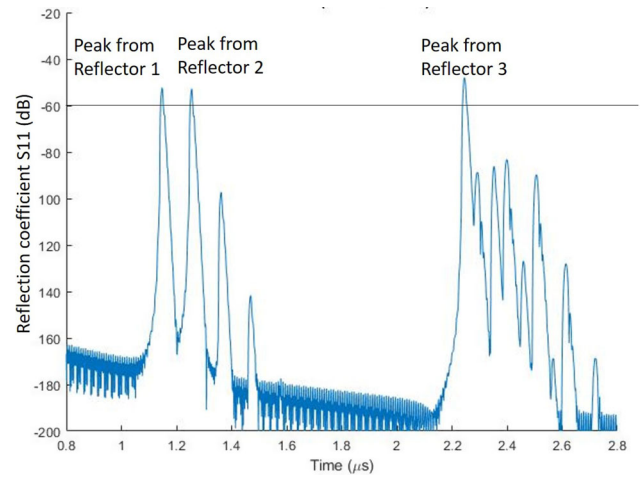


Figure 9. Simulated time response of the designed delay line. The three highest peaks above -60 correspond to the SAW reflection from the three reflector gratings. The weaker peaks emerge due to multiple reflections between the reflectors.

equal to two times the length of the IDT plus that of the reflector.

Aiming for the amplitudes of all echoes to be uniform, the finger number of reflectors was progressively adjusted. The response of the sensor, which is shown in Figure 9. Three reflection peaks higher than -60 dB appear in the time window ranging from 1.00 to 2.4 μ s, which stand for the reflections of SAW from the three reflector gratings. In addition, several relatively weaker peaks emerge due to multiple reflections between the reflectors.

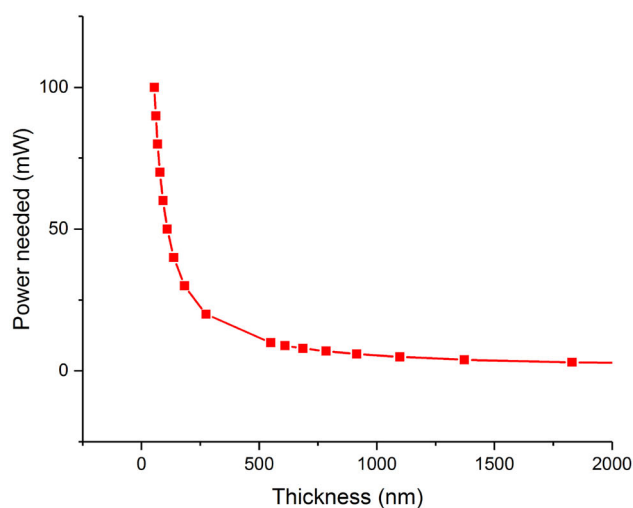
Gold layer

In order to achieve localized heating of the chip and avoid heat losses due to solid conduction in the sensor core, a Joule resistive layer was sputtered at the bottom side of the chip. The resistive layer of gold acts as a heater and receives current from the heating coil in its vicinity to which it is electrically connected.

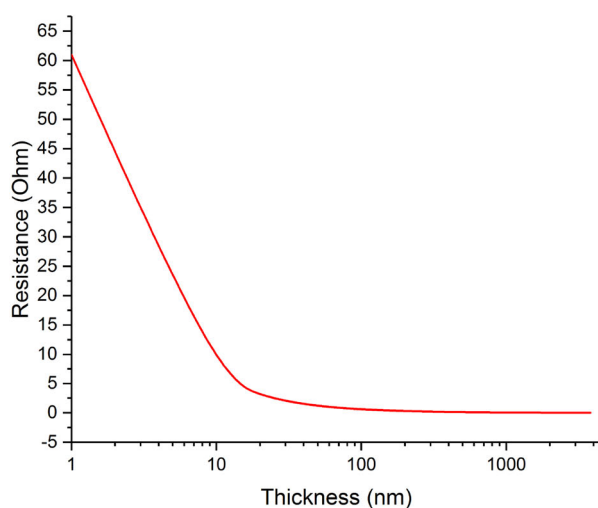
The value of the power consumption was determined by the simulation and equals to 24 mW. The current delivered by the coil was first simulated using the Wuerth Elektronik Red Expert Tool and the TINA software and then implemented and corresponds to 300 mA RMS. Taking those conditions into account and using Ohm's law it is possible to estimate the value of thickness needed.

$$R = \frac{rh}{wt} \quad (8)$$

where R is the resistance in Ω , r the resistivity in Ω m, h the length of the wire in m, w the width of the wire in m and t the thickness in m. A parametric



(a) Power vs thickness



(b) Resistance vs thickness

Figure 10. Power (a) and resistance (b) of the gold resistive layer vs thickness. A resistance higher than $1\ \Omega$ corresponds to a thickness lower than 10 nm. A power higher than 25 mW corresponds to a thickness lower than 250 nm.

study was performed varying the current, the power and the thickness of the gold layer while taking into account the manufacturing capabilities. A thickness of 100 nm corresponding to a resistance of $0.61\ \Omega$ was selected and later manufactured. The results obtained are plotted in Figure 10. Figure 10(a) displays the power received by the gold layer vs its thickness and Figure 10(b) displays its resistance vs thickness.

Coil

In order to operate properly the selected receiver coil from Wuerth Elektronik, a wireless power transfer circuit was designed and simulated prior to

Table 2. Electronic components used for the inductive coupling circuit.

Components	Values
MOSFET	IRLIZ44N
Resistor	12 k Ω , 1 k Ω , 1 Ω
Zener Diode	6.8 V and 5.1 V
Capacitor	100 μ F, 478 μ F, 47 μ F, 220 nF
Inductor coil	7.2 μ H
Potentiometer	100 k Ω
Power diode	0.1 A - 20 A

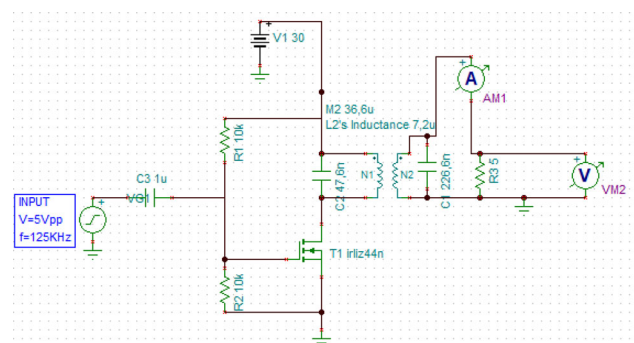


Figure 11. Wireless power transfer circuit for the heating unit. The transmitting circuit contains a $33.6\ \mu$ H coil connected in parallel to a $47.6\ \mu$ F capacitor. It is connected to a MOSFET IRLIZ44N supplied with 5 Vpp at 125 kHz. The receiving circuit is the receiver $7.2\ \mu$ H coil with the $226\ \text{nF}$ capacitor in parallel and a load resistance of $5\ \Omega$ representing the chip.

manufacturing and testing. A resonance frequency of 125 kHz was selected considering the operating range of the available Arbitrary Waveform Generator. Only a $226\ \text{nF}$ capacitor was connected in parallel to the receiver coil in addition to the sensing chip.

A wireless power transfer circuit using a MOSFET was designed and simulated using the TINA software. The NMOSFET (IRLIZ44N) was used in the transmitter circuit as an amplifier and the circuit was simulated using a transmitter coil of $33.6\ \mu$ H coil. It is connected to the MOSFET and to 2 resistors in parallel and to a capacitor. The receiver coil is connected in parallel to its $226\ \text{nF}$ coupling capacitor and to a load of $5\ \Omega$ that represents the sensing chip. The components used for the circuit are listed in Table 2 and the circuit is shown in Figure 11.

The circuit was provided with an input of 5 V peak to peak sine wave at a frequency of 125 kHz. By means of the voltage dividing circuit, the required amount of voltage is provided to the gate of the MOSFET to increase the voltage beyond the threshold value. The Drain of the MOSFET is connected to the transmitter coil and the receiver coil is connected with a capacitor in parallel. The output current across the receiver coil was measured using a $5\ \Omega$ resistor. The induction coupling coefficient between the

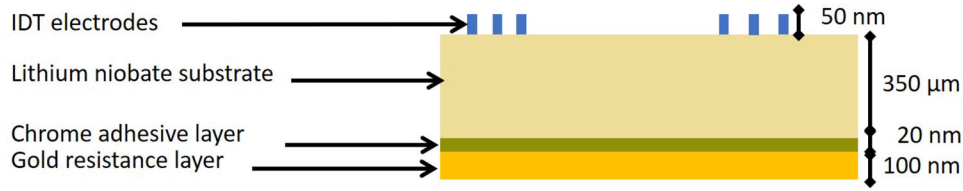


Figure 12. Layer structure of the chip. At the bottom of the chip a 20 nm adhesion layer of Chromium is sputtered followed by a 100 nm gold layer. On the top of the chip the IDT aluminum electrodes are etched by e-beam lithography.

primary and secondary coil was taken as 0.1 considering the small size of the receiving coil. A 1.2 V peak to peak voltage was measured at the resistance.

Manufacturing

The components simulated previously were manufactured and assembled together after some adjustments.

Sensing chip

The designed chip is 6 mm long, 400 μm wide and 350 μm thick and is a delay line. To assemble the first prototype, the SS24S2BB2 chip with similar properties manufactured by the company SAW Components (Dresden, Germany) was used. It is a 2.45 GHz resonator made of Lithium Niobate that has the same width and thickness as the designed chip, i.e., 400 μm by 350 μm. Only the length of 1 mm instead of 6 mm is different which makes the power transfer constraints for the first tests less stringent.

The IDT structure is generated via electron beam lithography. The structure of the IDT is similar to the one presented in [12], where a SAW chip was used as a temperature sensor operating at 2.45 GHz. The bare die on foil chip was ordered and was modified prior to its insertion inside the sensor. Three main operations were applied to it:

- the sputtering of the gold resistive layer at the bottom of the chip
- the soldering of the resistive layer to the rest of the sensor circuitry
- the wirebonding of the SAW IDT to connect it to the rest of the sensor

The three processes need to be compatible with each other [13], which means that the thickness of the gold layer needs to be compatible with the soldering and the adhesion between the gold layer and the lithium niobate crystal needs to be sufficient not to be ripped off during the soldering. For this reason a Chromium layer of 20 nm was evaporated between

the gold and the substrate which enabled the soldering. Figure 12 shows the layer structure of the chip.

The soldering was performed at the bottom side of the chip with Aluminum wire which was rather challenging due to the size of the chip (Figure 13(a)). The SAW IDT was connected to the rest of the sensor via ball wedge bonding. The chip was bonded to the PCB using a TPT Wirebonder. A 25 μm diameter wire at a temperature of 180 °C was wired by applying a force of 84 mN during 100 ms (Figure 13(c)).

The gold layer (Figure 13(b)) was sputtered using an UNIVEX 400 from the company Leybold and the electron beam evaporator Ferrotec-EVM-6. 20 nm of Chromium then 100 nm of gold at a speed of 10 rpm with no tilt angle were sputtered. In Figure 13, the results of the applied processes on the chip are depicted. The uniformity of the surface can be observed.

PCB

The heating unit of the sensor, i.e., mainly the coil and the interrogation unit, i.e., mainly the antenna were inserted together inside a PCB. The coil needs to be connected to a capacitor in parallel, the rest being done by the transmission circuit. The antenna needs a no ground surface around it of 9.5 mm² and a 50 Ω feed line. The PCB was designed using the software Sprint Layout and manufactured by the company Beta Layout.

Matching the impedance between the source and the load is important to obtain a better power transmission. The SAW chip and the antenna should be connected with a 50 Ω impedance trace. The track width corresponding to this was calculated using the following equation (obtained from <https://www.everythingrf.com/rf-calculators/microstrip-width-calculator>):

$$w = \frac{7.48 \times h1}{e^{\left(z_0 \frac{\sqrt{\epsilon_{r0}+4i}}{87}\right)}} - 1.25 \times t \quad (9)$$

where z_0 is the single ended impedance, ϵ_{r0} is the dielectric constant, w the width, t the trace thickness

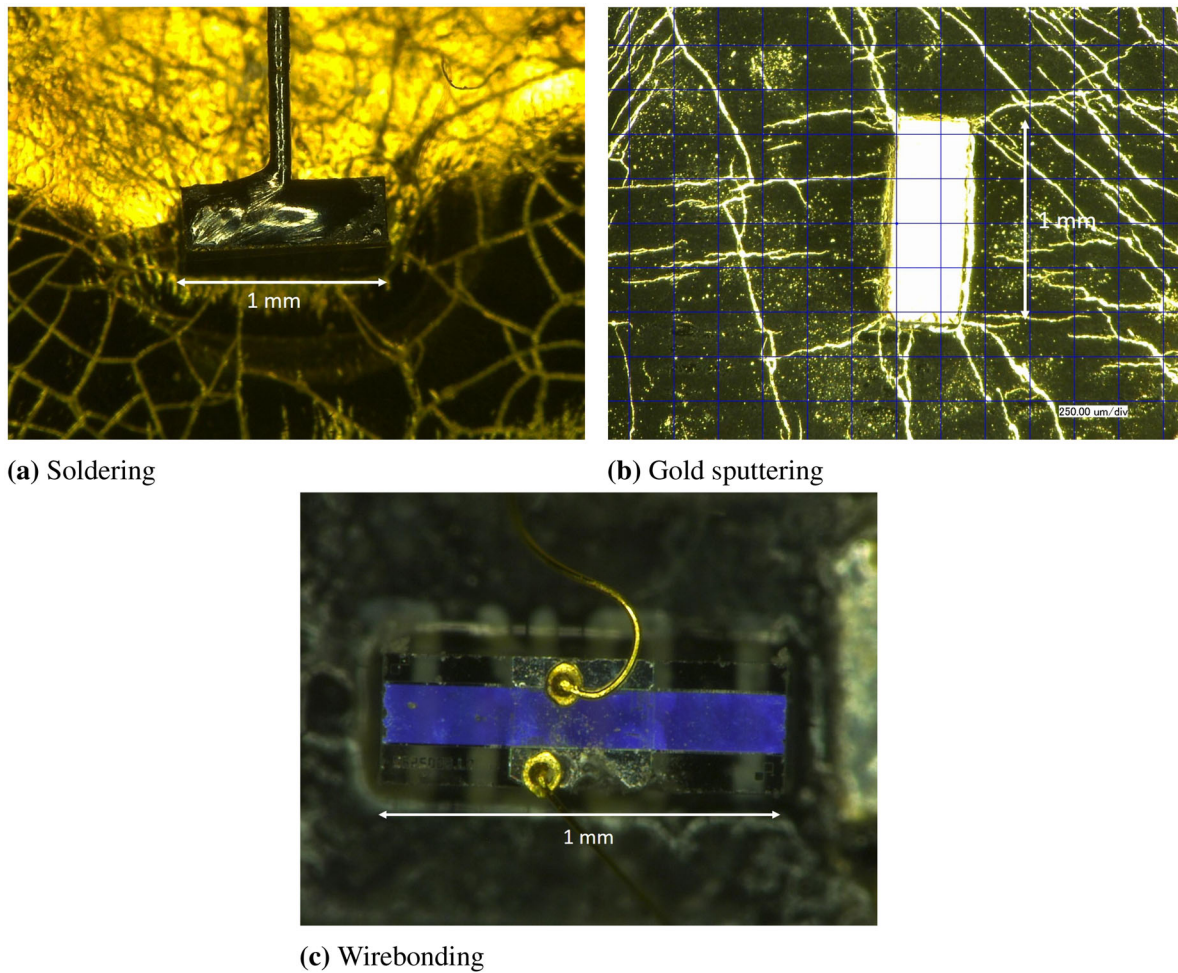


Figure 13. Manufacturing of the heating resistive layer and electrical contacting of the chip. Soldering (a) 100 μm diameter aluminum wire on the gold layer at the bottom of the chip, sputtering of the gold layer at the bottom of the chip (b) and wirebonding 25 μm gold wire on aluminum pad (c).

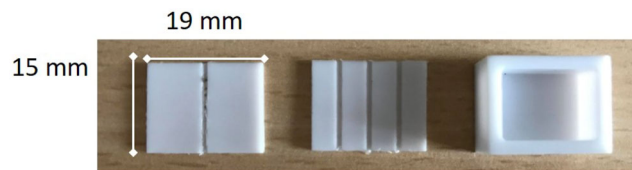


Figure 14. Sensor PTFE packaging. On the left the bottom part of the channel. On the middle the top part of the channel. The lateral channels are used for gluing. On the right side the cover that goes on top of the PCB is shown.

which equals 35 μm , h_1 the dielectric thickness of 0.38 mm. The resulting thickness is 0.642 mm.

Packaging

The packaging was designed in a way to enclose the PCB and the sensing chip. It was manufactured in three parts to allow a flexible mounting of the components. The lateral channels are made for gluing. The central channel has 4 holes for the wires to cross it. Figure 14 shows the manufactured packaging.

Discussion

Several manufacturing processes and technologies were combined to assemble the prototype of the sensor. Their compatibility with one another was assessed.

The choice of a delay line as the SAW IDT structure increases the length of the chip and therefore the Surface to Volume ratio and enables the identification of the sensor within a network. Indeed, the delay of the peaks due to the reflectors enables the RFID function.

In [7], Nicolay et al. implement a 10 mm by 3.1 mm by 1.8 mm SAW tag with a resistor glued on top of it which is more than 10 times bigger than the chip presented here. The heating is also performed by means of induction coupling providing current to the 35 Ω heating resistor. The transmitting coil is provided with a 10 V AC supply voltage at a frequency of 125 kHz. The receiving coil has an inductance of 10 μH and is connected in parallel to a 0.1 μF capacitor

to achieve the 125 kHz desired resonance frequency. The heating power provided to the resistor equals to 1.5 W whereas it equals 100 mW in our case. The coupling distance between the Tx and Rx coil is 15 mm against 10 mm in our case. In [7], the material of the vacuum window is fused quartz which has a dielectric constant of 3.78 whereas in our case, a PMMA window is used which has a dielectric constant of 3. The response time in [7] equals to 5 min whereas in the presented case it equals to 1 min approximately. Besides, according to the computations, the designed sensor should show a much higher sensitivity in the low pressure range.

In [10], which is the reported sensor that reaches the smallest vacuum pressure in the high vacuum range, the heating resistor consists of a membrane suspended by 4 beams of 70 μm width and 746 μm length. The chip has a 3 mm by 3 mm surface. The membrane material is Silicon Nitride. The heater is a Nickel thin film resistor patterned by lithography. In addition to that, a 100 nm thin film gold is deposited on both sides of the membrane area to reduce radiative heat transfer. The sensing range of the chip is 1.33×10^{-4} to 1332 Pa. A silicon microbridge acts as a heat sink in the same way as the microchannel in our case. Two different gas gaps are available on top and at the bottom of the chip. The top gap is 50 μm thick and the bottom gap is 300 μm thick.

In [14], an induction power transfer for brain implants is presented. The optimum link design efficiency reached is 80% and an efficiency of 20% is reached at 20 mm coupled distance by self-developed coils. In our case a 10% efficiency is reached at 10 mm distance due to the small size of the receiver coil.

In our design, the gold bonding wires have two functions: electrical connection of the chip to heating and interrogation units and mechanical support of the chip. The electrical connection is a conventional function of wires. However the mechanical support function induces supplementary requirements on the wires and the wirebonding process itself. In [15], process optimizations are performed on gold wirebonding in order to increase the yield and bond strength. Hardbaking and surface activation of the bonding pad improve the metal adhesion. The material of the bonding pad is also discussed. Thick electroplated gold bonding pad of 2 μm thickness should increase the mechanical stability of the wirebonding. In order to avoid failure modes such as delamination, optimized processes using commercial wirebonding technologies with no need for more equipment should be

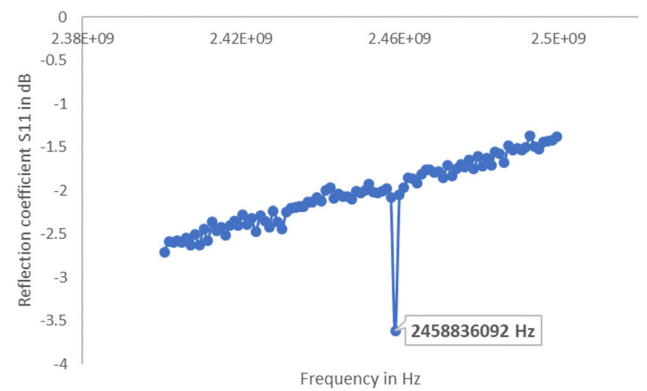


Figure 15. Reflection coefficient S11 vs frequency of the sensor at atmospheric pressure for a temperature of 21 °C. The SAW peak has a frequency of 2458836092 Hz.

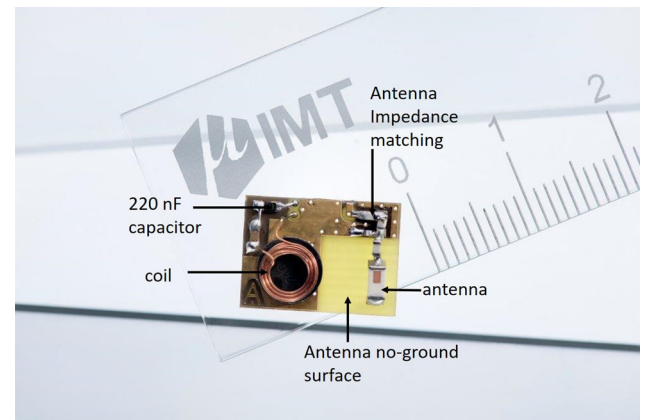


Figure 16. 15 mm by 11 mm by 3 mm PCB containing the heating unit and interrogation unit of the sensor.

sufficient. According to [16] Gold is the best material for semiconductor packaging compared to Copper, Silver or even Platinum. Indeed, Gold is the most stable and the most resistant to corrosion and requires less power and bonding force. However, for serial production, alloys based on copper or gold may be an alternative for cost saving.

All the designed components were manufactured and assembled. The antenna and coil were tested. The SAW chip was interrogated by means of the antenna using a frequency sweep between 2 and 3 GHz and the minimum of the reflection coefficient corresponding to the resonance frequency could be observed. The coil was tested and the output current of up to 1.2 V peak to peak could be measured at a 1 Ω resistance in series with the coil. The coupling distance between the transmitting and receiving coil was 6 mm.

The device was tested at room conditions (Figure 15) and still needs to be characterized in vacuum to determine its actual performances. All the operations

performed on the chip were successful. However, the soldering at the bottom of the chip destroyed the IDT structure at the top. The wires were able to support mechanically the suspended chip. The holes drilled on the packaging allowed the wires to connect the chip to the antenna and the coil. The PCB was designed in a way to minimize the length of the wires connecting the chip. [Figure 16](#) shows the manufactured PCB.

This means that the organization of the manufacturing steps that was adopted was not suitable. The main limitations and constraints came from the size of the chip. The chip was processed at its top and bottom side outside a clean room but preliminary results show that the designed structure is feasible as [Figure 13\(c\)](#) shows the processing of the chip at its top and [Figure 13\(a\)](#) shows the processing of the chip at its bottom. Indeed, the wirebonding, soldering and sputtering were challenging mostly due to the small size of the chip and many other technologies like electroplating were not possible for such a small chip.

The gold layer used as a resistive heating resistance is connected in series with the receiver coil which has a $0.44\ \Omega$ internal DC resistance at 293 K. This implies that the resistance of the gold layer has to be at least one order of magnitude higher in order to obtain significant signal and heat the chip, which means a value of the resistance higher than $4\ \Omega$. If the resistive layer is too thin the resistance value is sufficient but the wirebonding is not possible, if the resistive layer is too thick the wirebonding is possible but the value of the resistance is too low. The maximum thickness corresponding to a resistance of $5\ \Omega$ is 15 nm using [Equation \(9\)](#). Higher thicknesses could be electroplated but a larger surface is needed that is why if this is done at the wafer level higher values of thicknesses can be reached.

This means that a front end process performed at the wafer level and a better organization of the manufacturing steps is required. A solution to increase the resistance and the thickness at the same time is to make a meander resistor instead of a resistive layer. Since the IDT electrodes seem to be more fragile than the gold layer, they should be etched at last. The manufacturing steps of the chip could be:

1. Manufacture the meander resistor by laser etching
2. Wirebond the resistor and leave the wires suspended
3. Flip the wafer to process the top
4. Etch the IDT electrodes by e-beam lithography
5. Wirebond the IDT to the PCB

PTFE as a packaging material was a reasonable choice for a first prototype, however an improved version of the prototype could be made of Code 9658 ceramic for better stability in vacuum and a better protection of the chip.

The sensor operates via the transmission of two distinct waves. The antenna wave being in the Gigahertz range is more sensitive than the coil wave in the Kilohertz range. The position of the antenna inside the vacuum chamber is more critical and should be the closest to the outside environment. A coupling distance of 1 cm was reached between the Tx coil and the Rx coil but the coupling coefficient was very poor around 5%. Since the chip needs very few energy for heating, this is not an issue for operating the sensor. The same applies to the antenna, still the resonance of the antenna can be finely shifted using SU8 in order to match perfectly with the SAW peak frequency which would provide better quality signal.

A miniaturized wireless compact vacuum sensor was designed, simulated and a prototype was manufactured. The miniaturization of the heating and interrogation units in addition to the sensing chip raised some manufacturing and assembly challenges considering the semiconductor technologies currently available. All in all such a sensor is feasible provided a better manufacturing process is prepared. The obtained prototype will be tested in vacuum and the best operating mode still needs to be determined by acting on the input signal. Parameters of the input signal that will be varied are the AC signal form and the power input.

Conclusions

A new wireless vacuum sensor combining the Pirani principle and SAW was designed and simulated. The manufacturing processes needed for the prototype were identified and organized. This represents a step further toward the development of a completely miniaturized wireless vacuum sensor operating between high vacuum and atmospheric pressure. The quality of the manufacturing is critical to the performances of the sensor.

Funding

The authors would like to acknowledge the financial support provided by the EU network program H2020 under Grant MIGRATE No. 643095.

Notes on contributors



Sofia Toto is a Ph.D. student at the Karlsruhe Institute of Technology. Her thesis focuses on the development of a wireless vacuum SAW Pirani microsensors. She studied Mechanical Engineering at the Ecole Centrale de Nantes in France. In 2018, she was awarded the Elsevier Student Award for her research work during the European Vacuum Conference (EVC15) in Geneva. Her research interests include sensors, semiconductor technology and wireless telecommunications.



Pascal Nicolay received a B.S. degree in physics from Grenoble University in 1999, an Engineering Diploma from the Institut National Polytechnique de Lorraine in 2001 (ENSGSI), an M.S. degree in plasma physics, optics, electronics, and microsystems from Nancy University in 2004, and a Ph.D. degree in physics from Nancy University in 2007. From 2001 to 2004, he worked for the French Agency for Innovation (OSEO-ANVAR). He joined the LPMIA, Nancy, France as a Ph.D. student in 2004, where he worked on surface acoustic wave sensors, mainly for applications in the fields of high-temperature measurement and lowpressure monitoring. This work was made in collaboration with Doerler Mesures SA, in order to develop innovative and commercializable products. He is now with the Carinthia University of Applied Sciences, as a SAW researcher. He is currently interested in the modeling, design, and applications of electromechanical SAW components.



Gian Luca Morini graduated in Nuclear Engineering in 1992 and received a Ph.D. in Nuclear Engineering in 1996 from University of Bologna. He started as Assistant Professor at University of Ferrara in 1996. Since 2002 up to 2012, he was Associate Professor in Applied Thermal Engineering at the University of Bologna. Since 2005 he is Head of the Applied Thermal Engineering Laboratory of the DIN. He is author of 180 technical papers related to the Thermal Engineering and Heat Transfer.



Achim Voigt finished his degree as Diploma Engineer Physical Technology in 1991. He integrated the Karlsruhe Nuclear Research Center in 1992 and worked as Research and Development engineer for developing SAW based Gas and Bio Sensor Systems. Since 2006 he is at the Institute for Microstructure Technology (IMT) for engineering support of scientists and Ph.D. students. He took part to 10 KIT patents and owns one private patent.



Jan G. Korvink received his M.Sc. degree in mechanical engineering (specializing in computational mechanics) from the University of Cape Town, South Africa, in 1987, and his Ph.D. degree from the ETH-Zurich, Switzerland, in 1993. After completing graduation, he joined the Physical Electronics Laboratory, ETH Zurich. In 1997, he joined the University of Freiburg, Freiburg, Germany, as full professor for microsystems engineering. In Freiburg he co-directed the Freiburg Institute for Advanced Studies (FRIAS). In 2015 he joined the Karlsruhe Institute of Technology, where, besides directing the Institute of Microstructure Technology, he also acts as one of the speakers of the Helmholtz Program "Science and Technology of Nanosystems". He is the author or coauthor of more than 200 technical publications in the broad area of microsystems. He is a founding Editor of Advanced Micro and Nanosystems, and the co-founder of two successful startup companies. His research interests include the development of ultralow-cost micromanufacturing methods, microsystem applications in the area of magnetic resonance imaging, and the design and simulation of micro- and nanosystems. He was the recipient of a Red Dot Design Concept Award in 2011, and a European Research Council Advanced Grant in the area of micro NMR metabolomics for the nematode *C. elegans*.



Juergen J. Brandner studied Chemistry at University of Heidelberg and Electrical Engineering at Technical University of Karlsruhe (T.H.). He obtained his diploma in Electrical Engineering at the Technical University of Karlsruhe (T.H.) in cooperation with the Alternative Microstructuring Methods Research Group of the Karlsruhe Research Center. He obtained his Ph.D. in Mechanical Engineering from the Technical University of Karlsruhe (T.H.) with research on Fast Temperature Cycling of heterogeneously catalyzed gas phase reactions in microstructure devices. He is currently a lecturer for Micro Process Engineering at Dresden Technical University. He received his Habilitation and Venia legendi in Micro Process Engineering at Dresden Technical University.

References

- [1] J. Joseph, R. Nacereddine, M. Delanaye, J. Korvink, and J. Brandner, "Advanced numerical methodology to analyze high-temperature wire-net compact heat exchangers for a micro-combined heat and power system application," *Heat Transfer Eng.*, vol. 41, no. 11, pp. 1–13. DOI: [10.1080/01457632.2019.1589984](https://doi.org/10.1080/01457632.2019.1589984).
- [2] P. K. Weng, and J. S. Shie, "Micro pirani vacuum gauge," *Rev. Sci. Instrum.*, vol. 65, no. 2, pp. 492–499, 1994. DOI: [10.1063/1.1145163](https://doi.org/10.1063/1.1145163).
- [3] S. Dushman, *Scientific Foundations of Vacuum Technique*. New York, NY: Chapman & Hall, 1949.

- [4] D. Royer, and E. Dieulesaint, *Ondes élastiques dans les solides*. Paris, France: Masson, 1996.
- [5] D. Morgan, and E. Paige, *Surface Acoustic Wave Filters*. 2nd ed. Oxford, UK: Academic Press, 2007.
- [6] X. Liu, "Qi standard wireless power transfer technology development toward spatial freedom," *IEEE Circuits Syst. Mag.*, vol. 15, no. 2, pp. 32–39, 2015. DOI: [10.1109/MCAS.2015.2419011](https://doi.org/10.1109/MCAS.2015.2419011).
- [7] P. Nicolay, and M. Lenzhofner, "A wireless and passive low-pressure sensor," *Sensors*, vol. 14, no. 2, pp. 3065–3076, 2014. DOI: [10.3390/s140203065](https://doi.org/10.3390/s140203065).
- [8] D. Mercier *et al.*, "Characterization of a saw-pirani vacuum sensor for two different operating modes," *Sens. Actuators A: Phys.*, vol. 188, pp. 41–47, Dec. 2012. DOI: [10.1016/j.sna.2012.01.039](https://doi.org/10.1016/j.sna.2012.01.039).
- [9] S. Toto, P. Nicolay, G. L. Morini, M. Rapp, J. G. Korvink, and J. J. Brandner, "Design and simulation of a wireless sawpirani sensor with extended range and sensitivity," *Sensors*, vol. 19, no. 10, p. 2421, 2019. DOI: [10.3390/s19102421](https://doi.org/10.3390/s19102421).
- [10] F. Voelklein, M. Grau, A. Meier, G. Hemer, and L. Breuer, "Optimized mems pirani sensor with increased pressure measurement sensitivity in the fine and high vacuum regime," *J. Vac. Sci. Technol. A*, vol. 31, no. 6, pp. 061604, 2013. DOI: [10.1116/1.4819783](https://doi.org/10.1116/1.4819783).
- [11] V. Plessky, and J. Kosela, "Coupling-of-modes analysis of saw devices," *Int. J. High Speed Electron. Syst.*, vol. 10, no. 4, pp. 867–947, 2000. DOI: [10.1142/S0129156400000684](https://doi.org/10.1142/S0129156400000684).
- [12] C. Fu *et al.*, "Design and implementation of 2.45 ghz passive saw temperature sensors with bpsk coded rfid configuration," *Sensors*, vol. 17, no. 8, pp. 1849, 2017. DOI: [10.3390/s17081849](https://doi.org/10.3390/s17081849).
- [13] H. Reichl, "Packaging and interconnection of sensors," *Sens. Actuators A: Phys.*, vol. 25, no. 1–3, pp. 63–71, 1990. DOI: [10.1016/0924-4247\(90\)87010-G](https://doi.org/10.1016/0924-4247(90)87010-G).
- [14] S. Stoecklin, A. Yousaf, T. Volk, and L. Reindl, "Efficient wireless powering of biomedical sensor systems for multichannel brain implants," *IEEE Trans. Instrum. Meas.*, vol. 65, no. 4, pp. 754–764, Apr. 2016. DOI: [10.1109/TIM.2015.2482278](https://doi.org/10.1109/TIM.2015.2482278).
- [15] D. Sameoto, S. Lee, and M. Parameswaran, "Electrical interconnection through optimized wire-bonding onto SU-8 structures and actuators," *J. Micromech. Microeng.*, vol. 18, no. 7, pp. 075023, Jun. 2008.
- [16] C. L. Gan, U. Hashim, F. Classe, and B. L. Chan, "Future and technical considerations of gold wire-bonding in semiconductor packaging a review," *Microelectronics Int.*, vol. 31, pp. 121–128. Apr. 2014. DOI: [10.1108/MI-07-2013-0036](https://doi.org/10.1108/MI-07-2013-0036).